Journal Name

ARTICLE TYPE

Cite this: DOI: 10.1039/xxxxxxxxxx

Single nanoparticles magnetization curves by controlled tip magnetization magnetic force microscopy

Livia Angeloni,[a,b] Daniele Passeri,[*a] Davide Peddis,[c] Diego Mantovani,[b] and Marco Rossi[a,d]

Received Date
Accepted Date

DOI: 10.1039/xxxxxxxxxx

www.rsc.org/journalname

The development of high spatial resolution and element sensitive magnetic characterization techniques to quantitatively measure magnetic parameters of individual nanoparticles (NPs) is a hot topic in nanomagnetism to deeply understand and tune their magnetic properties. Magnetic force microscopy (MFM), thanks to its high lateral resolution, appears as a promising method for the magnetic characterization of single nano-sized materials although it is still limited by some drawbacks, above all the presence of electrostatic artifacts. Recently, these limitations have been overcome by the development of a particular MFM based technique, called controlled magnetization - MFM (CM-MFM) allowing, in principle, a quantifiable correlation between the measured magnetic signal and the magnetization of the studied object. Now we propose an experimental procedure, based on the use of CM-MFM technique, to measure the magnetization curve of single magnetic nanoparticles, individuating their saturation magnetization and magnetic field, and their coercivity. We measured for the first time the magnetization curves of individual Fe_3O_4 nanoparticles with diameters in the range of $21 - 32$ nm by using a MFM instrument. Results were in very good agreement with the quantitative data obtained by SQUID analysis on a macroscopic sample, showing the high potentiality of the technique in the field of nanomagnetometry.

The development of techniques for the magnetic characterization of nanoparticles (NPs) has become a fundamental need in nanomagnetism, because of the growing use of magnetic NPs (MNPs) in different technology fields, ranging from electronics (e.g., storage devices) [1] to environmental [2] and biomedicine applications [3–6]. The design and the optimization of these systems require a deep understanding of the mechanisms regulating the magnetism at the nanoscale. For example, several efforts are oriented to the individuation of precise relationships between the magnetic properties and numerous influencing morpho-structural and chemical parameters of NPs (e.g., the size, the shape, the chemical composition, and the crystal structure) [7–9], as well as to the comprehension of the influence of the mutual dipolar interactions between individual NPs, which depend on the magnetization state of the individual elements, the distance between them, their spatial configuration, and which, at the same time, affect the overall magnetic behavior of NPs based systems [10–13]. Ensemble measurements, such as superconducting quantum interference device (SQUID) [14], vibrating sample magnetometer (VSM) [15], and alternative gradient field magnetometer (AGFM) [16], are conventional methods successfully used to investigate the magnetic properties of NPs ensamble, such as patterns and ferrofluids, but, because of their 'macroscopic' character, allow one to relate the magnetic properties to other physical parameters only statistically. Therefore, an exhaustive understanding of the magnetic behavior of NPs, which requires the disembroiling of the complex interplay of the numerous influencing factors, appears to be achievable only by the use of high spatial resolution and element sensitive techniques, able to quantitatively measure the magnetic parameters of individual NPs. For this reason several efforts are focused on the research and development of new techniques with more and more high resolution, able to study the magnetic behavior of single, smaller and smaller, isolated nano-objects. Several techniques have been explored, but a standard method to quantitatively measure the main magnetic parameters of isolated nanomaterials has not been individuated yet.

The magnetization reversal of single micro and nanostructures can be, for example, characterized by different techniques such

[*] E-mail: daniele.passeri@uniroma1.it
[a] Department of Basic and Applied Sciences for Engineering, SAPIENZA University of Rome, Rome, Italy.
[b] Lab. for Biomaterials and Bioengineering (CRC-I), Dept. Min-Met-Materials Eng. & University Hospital Research Center, Laval University, Quebec City, Canada.
[c] Istituto di Struttura della Materia - CNR, 00016 Monterotondo Scalo, Rome, Italy.
[d] Research Center for Nanotechnology applied to Engineering of SAPIENZA University of Rome (CNIS), Rome, Italy.

as magnetoresistance techniques[17], spatially resolved Kerr effect (MOKE)[18], or magneto-optical scanning near field optical microscopy[19], but greater attention is paid to techniques having higher resolution and the capability of a more detailed study of the magnetization reversal of nanometer-sized NPs, like transmission electron microscopy (TEM) based techniques, such as differential phase contrast mode (DPC)[20] or off-axis electron holography[21,22], X-ray based techniques, such as soft X-ray spectroscopies, like X-ray holography[23] and transmission X-ray microscopy[24–26], ballistic Hall micro-magnetometry systems[27,28], micro and nano-SQUID[29–32], and X-ray photoemission electron microscopy (XPEEM)[33,34].

Nevertheless, all these techniques present some limitations, such as: the complex sample preparation procedures, typical of transmission electron techniques but also affecting nano-SQUID and ballistic Hall micro-magnetometry techniques, where the capability of measuring a single nano-object is related to the capability of placing that object in a determined area of the sensor, and, therefore, need additional instrumentation, such as nanomanipulators or atomic force microscopy (AFM) setups; the limited kind of analyzable materials as in the case of conventional X-ray microscopies, where only samples transparent to X-ray can be measured; the necessity of complex, expensive and not easily accessible instrumentation such as synchrotron facilities in XPEEM technique. For this reason research efforts are still addressed to the individuation of simple, user-friendly experimental setups which do not require complicated sample preparation, able to allow the study of any kind of magnetic nanomaterials and to furnish quantitative information about the magnetic parameters of the selected element.

Magnetic force microscopy (MFM) is a scanning probe microscopy technique, able to simultaneously acquire the morphology of a surface and map the magnetic interaction forces between the tip and the sample with nanometer spatial resolution. These capabilities, together with the possibility of equipping commercial MFM instruments with systems (electromagnets) able to produce adjustable magnetic fields both perpendicular (out-of-plane) and parallel (in-plane) to the sample surface, make MFM an effective and widely used tool for the qualitative study of the magnetic characteristics of single nanoparticles[35–39], also in response to the application of external magnetic fields[40]. Nevertheless, the potentialities of MFM in the measurement of quantitative magnetic parameters (such as the saturation magnetization M_s, the saturation magnetic field H_s, the coercivity H_c and the magnetization reversal curve) of single objects at the nanometer scale have still not been completely exploited and only few results are available. Indeed, nowadays, the only commonly used quantitative MFM procedure is the local statistical measurement of the switching field distribution and the remanent or 'in field' hysteresis curves of bit-patterned recording media, consisting in arrays of nanodots[41–43], nanoislands[44], nanowires and nanotubes[45,46], which is generally performed by applying controlled out-of-plane magnetic fields to the sample and counting the number of magnetically reversed entities. Concerning the quantitative measurements of magnetic properties of single nanomaterials, the hysteresis loop of individual nanowires both under parallel and perpendicular magnetic fields has been measured by MFM[47]. Indeed, in the case of bistable magnetic nanomaterials with high magnetic moment (such as nanowires), the magnetization state of the sample can be easily visualized on MFM images as an alternation of 'bright' and 'dark' contrast (i.e., repulsive and attractive tip-NP interaction). Therefore, the magnetization curve (and the definition of quantitative magnetic parameters) of a single element can be obtained acquiring several images with different external magnetic fields[47] or by recording only one MFM image continuously varying the applied magnetic field during the scan[48] and then plotting the contrast between two points (dark/bright contrast) in a selected line or region as a function of the applied magnetic field. Similarly, the magnetization curve of single nanodots in response to out-of-plane and in-plane magnetic fields has been measured using MFM by plotting the nanodot average phase (or frequency/amplitude) shift as a function of the applied magnetic field[49] or by acquiring the MFM contrast in a single scan line while continuously varying the applied field[50]. These methods have been successfully applied to dots having size ranging from 200 nm to 20 μm. Nevertheless, in the case of superparamagnetic nanoparticles having size less than 100 nm, the magnetization reversal behavior of single NPs has been studied only qualitatively[40]. Only Sievers *et al.*[51] and Schreiber *et al.*[39] succeeded in retrieving the magnetic moment of nanoparticles from standard MFM images describing the tip-NP interaction as the force occurring between two magnetic dipoles, while other authors did not find any correlation between the experimental MFM data and the proposed 'dipole' model[36,52,53]. As already highlighted in the literature[35], these incongruities can be ascribed to several factors, which make magnetic nanoparticles with size lower than 100 nm a challenging sample to be quantitatively analyzed by MFM. These factors can be summarized as: i) the low magnetic moment, which produces a low magnetic tip-sample interaction, close to the sensitivity limit of the technique; ii) the presence, in MFM images, of an additional signal due to electrostatic tip-sample interactions (i.e., van der Waals, electric charge, capacitance coupling), which has been demonstrated to be of the same order of magnitude in respect to the magnetic one[35]; iii) the lack of an unambiguous theoretical model describing the tip-sample (NP) interaction consistently with experimental data and the consequent difficulty in converting the detected MFM signal to the quantitative value of a physical parameter, such as the magnetic moment of a single nanoparticle. Some methods to remove the electrostatic effects in MFM images have been proposed, such as the combined use of Kelvin probe force microscopy and MFM, proposed by Jaafar *et al.*[54], or the switching probe magnetization MFM and the differential MFM, proposed by Cambpel *et al.* and Wang *et al.*, respectively[55–57].

Recently, we proposed a new MFM technique, called controlled magnetization-MFM (CM-MFM), with the aim of depurating the MFM signal from the electrostatic artifacts and detecting the signal due to the sole magnetic tip-NPs interactions[58]. The analysis of superparamagnetic nanoparticles through the use of CM-MFM showed that, once the electrostatic artifacts are removed from the MFM data and the 'pure magnetic signal' is detected, the tip-NP interaction can be simply described by the magnetic interactions

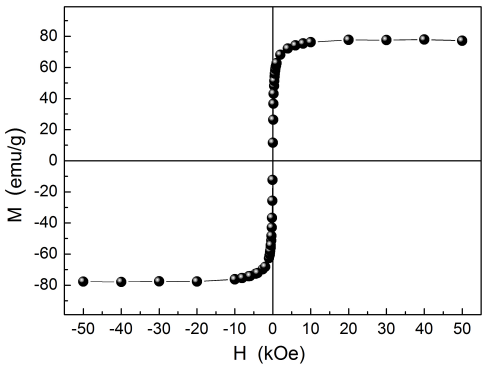

Fig. 1 Magnetization curve obtained on magnetite NPs by SQUID.

between two single-point magnetic dipoles placed close to the geometrical center of the tip apex and the NP, respectively[58]. This result has confirmed the possibility of extrapolating quantitative information about the magnetic properties of nanoparticles from MFM measurements, providing that electrostatic effects are eliminated, which is an essential step of the method.

In this work we propose a MFM based, which is based on CM-MFM previously described[58] but takes advantage of the application of an additional smaller magnetic field during the experiment, to quantitatively retrieve the magnetization curve of single magnetic nanoparticles by in-field CM-MFM measurements. The procedure has been tested on Fe_3O_4 NPs and the obtained results have been compared with standard magnetometry to assess the effectiveness of the proposed technique.

1 Materials and methods

1.1 Controlled magnetization magnetic force microscopy

As previously described[58], CM-MFM consists in the acquisition of two MFM images with two different magnetization state of the probe. Each MFM image is acquired using the standard MFM 'lift height mode', consisting in a double scan of the sample area: the first scan is performed in tapping mode in order to acquire and record the topography profile of the sample; the second scan is performed in dynamic non-contact mode with the tip following a trajectory corresponding to the previously recorded sample profile, with the aim of recording the phase (or frequency) shift map due to the tip-sample long-range interaction forces F experienced in each point of the scanned area. In particular, the phase shift $\Delta\varphi$ is given by the relation

$$\Delta\varphi = -\frac{Q_c}{k_c}\frac{\partial F_z}{\partial z} \quad , \tag{1}$$

where Q_c and k_c are the quality factor of the cantilever first resonance in air and the cantilever spring constant, respectively, and $\partial F_z/\partial z$ is the gradient along the z direction perpendicular to the surface plane of the component along z of the long-range interaction force F_z. In CM-MFM, a first standard MFM image ($\Delta\varphi_{MagnTip}$) is acquired with the probe magnetized in its saturation magnetization state ($M_{rs,tip}$). This image is given by the superimposition of the signals due to both magnetic ($\Delta\varphi_{magn}$) and electrostatic ($\Delta\varphi_{el}$) tip-sample interaction forces[58]. Then, the tip can be demagnetized through the application (and the switching off) of its coercive remanent field $-H_{rc,tip}$, previously determined by a probe calibration procedure, and a second image is acquired with zero probe magnetization and with the same scanning parameters ($\Delta\varphi_{DemagnTip}$), in order to detect only the electrostatic contribution ($\Delta\varphi_{el}$). Therefore the MFM signal due to only magnetostatic tip-sample interactions is obtained by subtracting the second image to the first one, being $\Delta\varphi_{magn} = \Delta\varphi_{MagnTip} - \Delta\varphi_{DemagnTip}$.

In this work, CM-MFM has been performed using a standard MFM instrumental apparatus (Icon, Bruker Inc.) equipped with a standard CoCr coated silicon cantilever (MESP, Bruker Inc.). From the analysis of the first free mode of the cantilever in air, the resonance quality factor $Q_c = 190$ and the cantilever spring constant $k_c = 1.0$ N/m were determined. The MFM setup was equipped with an electromagnet placed under the sample. This configuration allows the tuning of the magnetization state of the probe, through the application and the switching off of opportune out-of-plane magnetic fields as previously described[58], i.e., the implementation of CM-MFM technique, and the tuning of the 'in field' (out-of-plane) magnetization state of the sample through the application of controllable out-of-plane magnetic fields during the scan (and, therefore, the study of the magnetization state of the sample in response to an external magnetic field). The range of possible magnetic fields applicable with the used instrumentation is -480 Oe $< H <$ +480 Oe, which has been demonstrated to be appropriate to saturate and nullify the magnetization of standard commercially available MFM probes[58]. The in situ demagnetization of the probe, necessary to perform CM-MFM, has to be obtained by applying to the magnetized tip its previously measured remanent coercive field $H_{rc,tip}$. Therefore, a preliminary calibration phase has been necessary. Using a floppy disk as a reference sample, the remanent magnetization curve of the probe has been measured (and thus the saturation magnetic field $H_{rs,tip}$ and the coercive field $H_{rc,tip}$ have been determined) by plotting, as a function of the magnetic field, the phase contrast measured between two adjacent domains after applying and switching off magnetic fields with different intensities. The detailed 'probe calibration' procedure has been previously reported[58]. All the measurements reported in this work have been carried with the same probe for which the values of $H_{rs,tip} = 440$ Oe and $H_{rc,tip} = 230$ Oe have been found. In-field measurements have been performed by applying an out-of-plane external magnetic H_{ext} field in the range -10 Oe $< H_{ext} <$ +65 Oe and at $\Delta z = 100$ nm.

1.2 Materials and ancillary techniques

In order to validate the proposed measurement procedure, a sample of commercially available magnetite NPs (Sigma Aldrich) with nominal average diameter of 30 nm have been studied. The sample was diluted in distilled water and a drop of the resulting dispersion was placed on a silicon single crystal substrate. Measurements were performed after complete evaporation of the water.

The global magnetic characteristics of the sample were studied

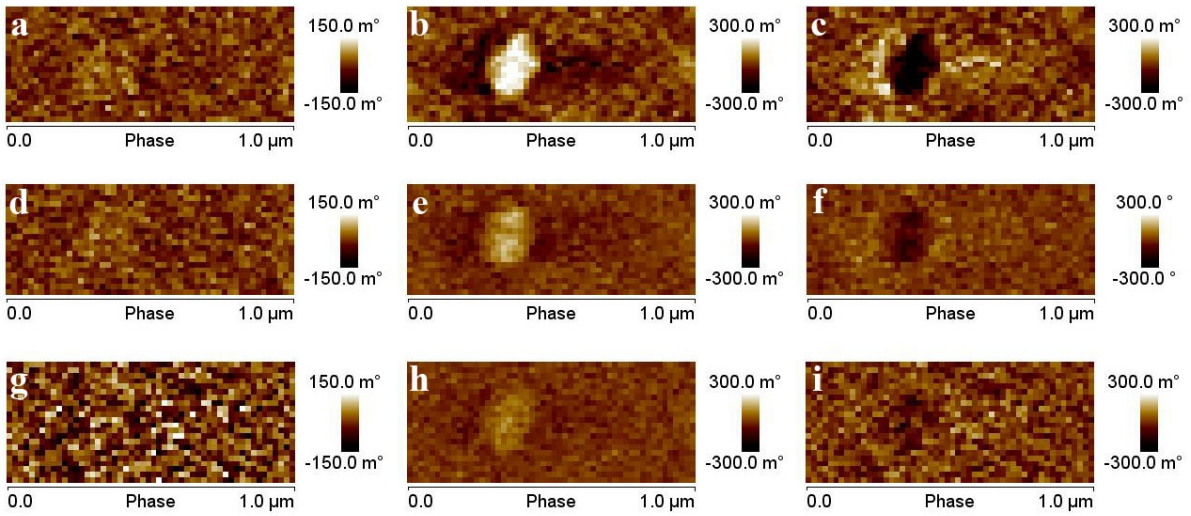

Fig. 2 Standard MFM images (a, d, g), electrostatic images (b, c, h) and CM-MFM images (c, f, i) at lift height Δz of 20 nm (a, b, c), 50 nm (d, e, f) and 80 nm (g, h, i) of a NP of 31 nm diameter.

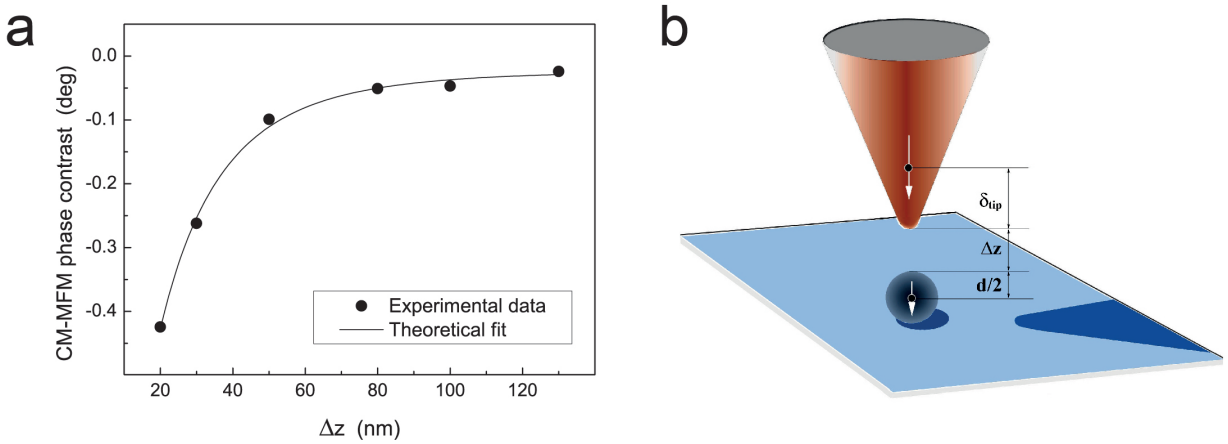

Fig. 3 (a) CM-MFM phase-distance curve (symbols) and theoretical fit (solid line); (b) sketch of the equivalent two-dipole model describing the tip-NP interaction.

using SQUID. Macroscopic DC magnetization measurements were performed using a SQUID magnetometer equipped with a superconducting coil ($H_{max} = \pm 5$ T). To avoid any movement of the NPs during the measurements, the samples, in the form of powders, were immobilized in epoxy resin. The obtained magnetization curve is reported in Fig. 1, from which the saturation magnetization $M_s = 78$ emu/g is calculated, reached at a saturation field of about 10^3 Oe.

2 CM-MFM procedure for the measurement of single NPs magnetization curves

The CM-MFM procedure we propose to measure the magnetization curves of single magnetic nanoparticles consists in two phases: i) the acquisition of the magnetic phase signal as a function of the tip-sample distance (i.e., the lift height) on different NPs, in order to calibrate the magnetic parameters of the tip; ii) acquisition of the magnetic phase signal as a function of the applied magnetic field of isolated NPs and conversion of obtained curves into magnetization curves of each NP.

2.1 Calibration of the magnetic parameters of the tip

Different CM-MFM images of NPs, resulting from the subtraction of the images obtained with the demagnetized probe to the corresponding standard MFM images, are acquired in correspondence of different lift heights (i.e., the distance between the probe and the sample). In Figure 2, an example of standard MFM images, the electrostatic images and CM-MFM (magnetic) images of a Fe_3O_4 NP having diameter, evaluated from the corresponding AFM topography (image not shown), of 31 nm acquired at different lift height values are shown. The value of the diameter, in good agreement with the specifications supplied by the producer, indicate the analyzed NP is isolated and not an agglomerate of smaller NPs, and it is representative of the NPs population. As expected and already observed in previous works[58,59], in electrostatic phase images, NPs exhibit positive phase contrast (in respect to the substrate), the intensity of which decreases with the increase of the tip-sample distance, pointing out the presence of detectable non-magnetic tip-NP interactions. The standard MFM images also show a positive contrast in correspondence of NPs, but lower than the corresponding electrostatic signal highlighting the presence of a magnetic effect (which, in the absence of an external magnetic field and in the case of superparamagnetic NPs, should give rise to a negative phase contrast contribution due to the attractive tip-NP interaction), which is 'hidden' by the predominant electrostatic signal and become visible only after its subtraction in CM-MFM images. Indeed, CM-MFM images exhibit negative contrast in correspondence of NPs, which decreases with the increase of the tip-sample distance. By measuring, for each tip-sample distance, the CM-MFM phase shift difference between the apex of the magnetic NP and the substrate and by plotting the obtained values as a function of the tip-sample distance (lift height), the magnetic phase-distance curve for each measured NP is obtained, an example of which is reported in Fig. 3a. In absence of electrostatic artifacts, the tip-NP interaction can be described using the two-dipole model as sketched in Fig. 3b, where both the tip and the NP are described as two single point magnetic dipoles[58]. The magnetic phase shift can be obtained as

$$\Delta\varphi = \mu_0 m_{tip} M_{NP} \frac{Q_c}{k_c} \frac{d^3}{\left(\Delta z + c_s + d/2 + A_{sp} + \delta_{tip}\right)^5} \quad , \qquad (2)$$

where: μ_0 is the permeability of free space; Q_c and k_c are the quality factor and the spring constant of the used cantilever, respectively, which can be evaluated from the cantilever first free resonance in air; A_{sp} and Δz are the amplitude set point and the lift height selected for the specific measurement (and, therefore, are known); d is the NP diameter, measured as the NP height in topography images; c_s the thickness of the possible non-magnetic coating of the NP (which is 0 in the case of this work); M_{NP} is the magnetization of the NP; δ_{tip} is the position, in respect to the tip apex, of the equivalent magnetic dipole of the probe having momentum m_{tip}. The tip momentum m_{tip} and its equivalent position δ_{tip} are not known a priori and have to be determined. By fitting the $\Delta\varphi$ versus Δz experimental curves using Equation 2, e.g., symbold and solid line in Fig. 3a, respectively, δ_{tip} can be evaluated. We repeated this procedure on 6 different NPs with different diameters, obtaining $\delta_{tip} + A_{sp} = 104 \pm 24$ nm.

2.2 Magnetization curves measurement

After selecting an opportune lift height, different 'in-field' MFM images (using the magnetized probe) of an isolated NP are acquired in correspondence of different intensities of out-of-plane magnetic fields (H_{ext}) applied during the scan. At the same lift height, the pure electrostatic image corresponding to each NP is acquired with the demagnetized probe at $H_{ext} = 0$ and subtracted to the corresponding MFM image, allowing the measurement of the 'pure' magnetic phase signal (corresponding to the apex of the NP) as a function of the applied magnetic field. As an example, in Fig. 4 a series of images obtained on a Fe_3O_4 NP of 31 nm diameter applying the described procedure, at lift height of 100 nm, is shown, and in particular: the topography (a), the electrostatic image at $H_{ext} = 0$ (b), the series of standard MFM images for different intensities of the applied magnetic field (c, e, g) and the series of corresponding CM-MFM images (d, f, h). The corresponding MFM and CM-MFM phase versus the applied magnetic field curves are reported in Fig. 5a and b, respectively. As visible in MFM images and in the MFM phase versus H_{ext} curves, in standard MFM images NPs exhibit a positive contrast, which is constant in correspondence of high magnetic fields (higher than 60Oe), decreasing with the decrease of the applied magnetic field, and reaches a constant value (close to zero) at about 20 Oe and lower magnetic fields intensities. Similar behavior has been observed inverting the direction of the applied magnetic fields. The reaching of a constant (saturation) value in correspondence of the highest and lowest magnetic fields values and the decrease/increase of the phase contrast with the decrease/increase of the applied magnetic field in the intermediate range indicates a relationship of the phase contrast trend with the magnetization reversal behavior, which can be also recognized observing the curve of the measured MFM phase contrast as a function of the applied field, reported, as an example, in Fig. 5a.

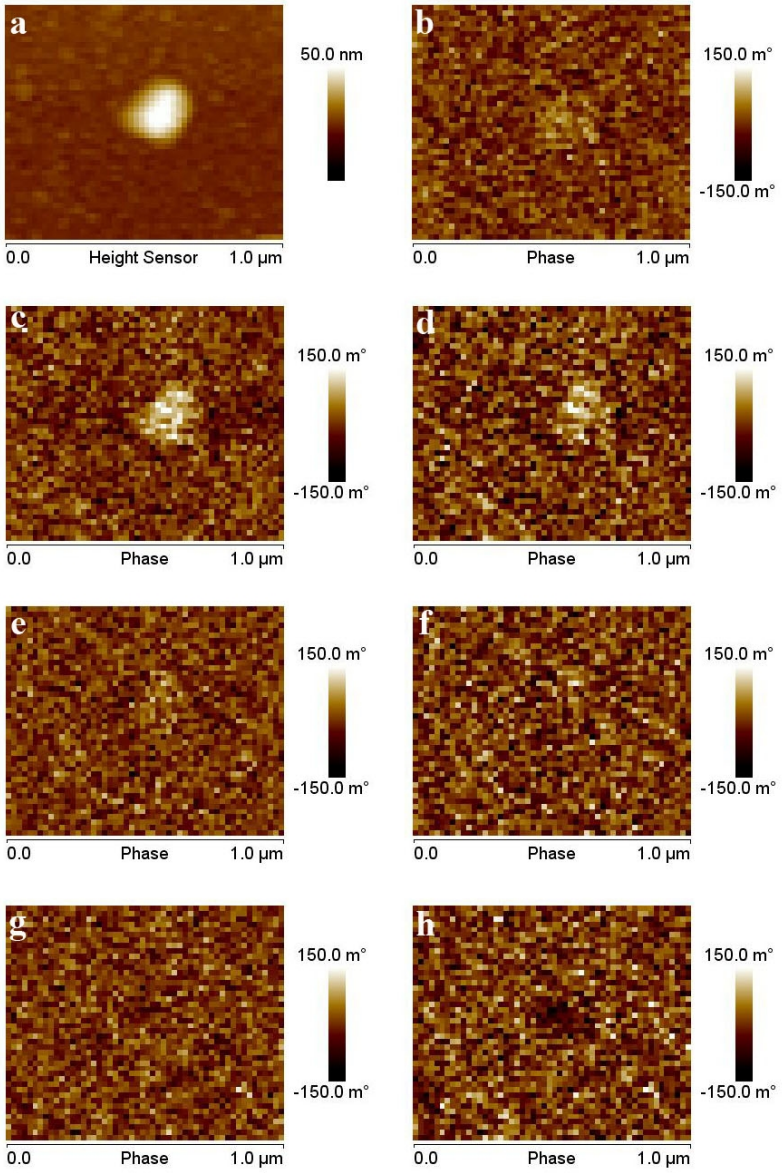

Fig. 4 Topography (a), electrostatic image at $\Delta z = 100$ nm and $H_{ext} = 0$ (b), standard MFM images (c, e, g) and corresponding CM-MFM images (d, f, h) at $H_{ext} = +60$ Oe (c, d), $H_{ext} = +19$ Oe (e, f) and $H_{ext} = -10$ Oe (g, h) of a NP of 31 nm diameter.

Nevertheless, an inversion of the contrast (i.e., an inversion of the magnetization) should occur in correspondence of the reversal of the applied magnetic field. This is not observable in standard MFM images, which, indeed, give rise to a MFM phase versus applied magnetic field curve completely asymmetric in respect of both the two axes by reason of two phenomena. The first one, responsible for the fact that an inversion of the phase contrast is not visible at all in standard MFM images, is the presence of electrostatic artifacts, the effect of which is visible when comparing the MFM images with the correspondent electrostatic one. Indeed, the positive contrast detected in standard MFM images is higher than the electrostatic contrast in correspondence of high magnetic fields and lower than the electrostatic contrast in correspondence of low magnetic fields. After subtracting the electrostatic effects to MFM images (which corresponds to the subtraction of a phase shift bias from the MFM phase contrast data in Fig. 5a), an inversion of the contrast in correspondence of a value of magnetic field approximately intermediate between the two 'saturation' magnetic field values is clearly visible in CM-MFM images, where the NP phase contrast is positive in correspondence of high magnetic fields and negative in images acquired at low magnetic fields. This confirms, not only the actual correspondence between the in-field CM-MFM data with the magnetization reversal curve of a NP, but also the accuracy of the measured electrostatic signal, indicated by the symmetry, in respect to the y-axis, of the curve obtained after the subtraction of the non-magnetic contribution, as shown in the curve reported in Fig. 5b. Nevertheless, as visible in both CM-MFM images and in the curve of the CM-MFM phase as a function of the applied magnetic field, the contrast inversion occurs in correspondence of magnetic field values very different from zero. This is due to the fact that the external magnetic field we apply is not the only one affecting the magnetization state of the sample, but also the magnetic stray field of the probe H_{tip} is present and produces an additional contribution to H_{ext}. This additional contribution can be, therefore, evaluated as the H_{ext} value corresponding to the center of the measured curve. From the value of H_{tip}, which we found as high as 33 ± 2 Oe, the value of m_{tip} can be obtained from the relation

$$H_{tip} = \frac{1}{2\pi} \frac{m_{tip}}{\left(\Delta z + c_s + d/2 + A_{sp} + \delta_{tip}\right)^3} \quad , \tag{3}$$

which gives $m_{tip} = (1.7 \pm 0.4) \times 10^{-13}$ emu, in very good agreement with the (approximated) value of 1×10^{-13} emu supplied by the producer. The single NP magnetization curve can be thus obtained converting the measured magnetic phase contrast in the corresponding magnetization values (M_{NP}) using Equation 2, which actually corresponds to multiplying the CM-MFM phase contrast data in Fig. 5b by a constant value. As an example, Fig. 5c shows the calculated magnetization curve obtained from the CM-MFM phase versus H_{ext} curve reported in Fig. 5b.

3 Results and discussion

The described procedure has been applied to four Fe_3O_4 NPs. In Table 1, the obtained values of saturation magnetization (M_s) and coercive field (H_c) of the measured four magnetite NPs, with diameters in the range 21-32 nm, are reported. The values of M_s and the corresponding uncertainties are calculated from the two saturation magnetization values found for each curve, i.e., for positive and negative values of H_{ext}. All the values of M_s measured for the four NPs are in satisfyingly good agreement with the value of $M_s = 78$ emu/g measured with SQUID, considering that the latter is averaged on the whole population of NPs, and with the values of saturation magnetization of magnetite NPs reported in literature ($55 - 92$ emu/g)[60–64]. Moreover, when calculating the weighted average value of saturation magnetization (using the mass of each NP as the weight in the average), 75 ± 5 emu/g is obtained which is in very good agreement with SQUID data.

Table 1 Parameters obtained from the magnetization curves of four different NPs: for each NP with diameter d, the saturation magnetization M_s and the coercivity H_c are reported.

d (nm)	M_s (emu/g)	H_c (Oe)
32	64 ± 4	5.5 ± 2.0
31	68 ± 1	6.5 ± 2.0
25	78 ± 23	0
21	131 ± 10	0

Observing the values obtained in correspondence of the single NPs and their uncertainties, it is possible to note that the NPs with diameters around 30 nm (which is the nominal average diameter of the analyzed NPs) exhibit saturation magnetization values close to the literature values[60–63] and to the value obtained by SQUID. Furthermore, the small error indicates a high symmetry of the obtained curves (as also observable in Fig. 5, where the curve obtained for the NP with diameter of 31 nm is shown). These results seem to show the good operation of the technique for particles having diameter higher than 30 nm. The 25 nm sized NP shows a saturation magnetization in very good agreement with the value measured with SQUID and with the values reported in the literature. The high error indicates a significant asymmetry of the curve, which demonstrates a not accurate evaluation of the electrostatic signal in this case. A significantly higher value of saturation magnetization has been observed in correspondence of the smaller NP (21 nm). The significant and unexpected increasing of the saturation magnetization with the decreasing of the NP size could be due not to a real effect but to some limits of our procedure which could become particularly critical when the NP size decreases under a certain dimension. More specifically, in our previous works, we estimated that, with the present settings and equipment, our technique could be suitable for the study of NPs with diameter not smaller than 10 nm, being 10^{-2} deg the minimum value of detectable phase[58]. Nevertheless, also in correspondence of slightly higher dimensions, the magnetic sensitivity and the quantitative accuracy of the measurements are inevitably reduced. Furthermore, the volume of the NPs has been calculated considering the NPs having spherical size. This approximation, especially for very small NPs could be not realistic.

Also, it is worth noting that from Fig. 5 the magnetic field H_{sat} required to saturate the magnetization of the NP is about 25 Oe. An analogous result is obtained for all magnetization curves we acquired. This result is somehow surprising if compared to the

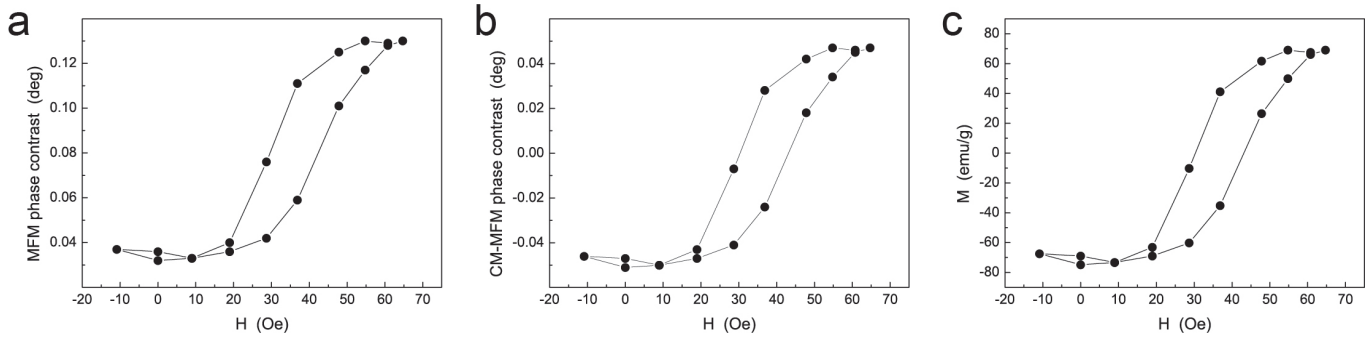

Fig. 5 (a) MFM phase versus applied magnetic field curve at $\Delta z = 100$ nm of a NP of diameter of 31 nm; (b) corresponding CM-MFM phase versus applied magnetic field curve; (c) corresponding magnetization versus applied magnetic field curve.

values of saturation field obtained by SQUID and commonly reported in literature, which are about 50 times bigger. Although this result deserves further investigation, we believe that a first attempt of rationalization can be done considering that NPs in our sample are much more diluted than in samples usually characterized with SQUID. Thus, the mutual interactions among NPs, which lead to a reduction of the effective magnetic field experienced by each NP, are negligible in our case. Therefore, we believe that saturation fields measured with 'global' techniques are actually overestimated due to not negligible magnetic interactions among magnetized NPs.

Finally, the analysis of coercive field (H_c) of the measured NPs highlighted the presence of a certain hysteresis and thus a certain coercivity, in correspondence of bigger NPs (31 and 32 nm of diameter), while no coercivity has been detected in correspondence of NPs having diameter lower than 25 nm, which therefore seem to exhibit a superparamagnetic behavior. Although additional and more accurate experiments are required also considering the relatively high uncertainty in the results here presented, the observation of a 'threshold effect' seems to confirm results already reported in literature, where an analogous effect was observed using standard 'global' techniques for the coercivity of magnetite NPs in the range between 25 and 15 nm[60]. Our results demonstrate that CM-MFM is a powerful technique for the magnetic characterization of single nanomaterials, allowing one to obtain the actual magnetization curve of the investigated nano-object. However, some issues still limiting the accuracy of our technique have to be addressed. Indeed, in addition to the limitation to the accuracy due to the experimental setup, e.g., the limited sensitivity of the power supply and the related possibility of not complete demagnetization of the tip[58], the analytical model used in the tip calibration should be improved, as the value of δ_{tip} retrieved from the fitting procedure shows a relatively high variation among different NPs. Conversely, the estimation of H_{tip} is very accurate as it does not sensibly vary among different NPs. Nevertheless, the uncertainty in δ_{tip} results in an increased uncertainty in the values of m_{tip} estimated from H_{tip} using Equation 3. In addition, the incorrect evaluation of electrostatic forces, mainly due to a residual magnetization of the tip in its demagnetized state[58], may lead to asymmetric magnetization curves. This effect seems more dramatic in case of small NPs. Finally, the calculation of the magnetization is performed assuming a spherical geometry for the NPs which may be not correct in case of small NPs. This assumption may result in an incorrect calculation of the NP volume and thus of the magnetization. While the spherical assumption can be checked in case of bigger NPs from the topographical images, in case of smaller NPs the true geometry is difficult to assess due to the effect of tip convolution. Notwithstanding these current limitations which have to be addressed, however, CM-MFM has been proved a powerful technique for the local nanomagnetic characterization of single nanomaterials.

4 Conclusions

An experimental procedure, consisting of a series of in-field CM-MFM measurements aimed to the reconstruction of the magnetic phase versus the tip-sample distance and versus the applied external magnetic field, and a data post-processing method for the quantitative magnetic characterization of single NPs have been proposed, described and discussed in this work. The use of CM-MFM allowed us to obtain the signal originating from the sole magnetic tip-NP interaction, after subtracting the contributions due to any non-magnetic force. Consistently with previous results, the detected pure magnetic signal resulted well interpreted by the theoretical model describing the magnetic tip-NP interaction force as the interaction between two magnetic dipoles, confirming the correctness of the CM-MFM working principle. By fitting the measured magnetic phase versus distance curves and analyzing the information about the probe stray field retrieved from the measured magnetic phase versus applied magnetic field curves, we were able to calculate the unknown magnetic parameters of the used probe (i.e., the magnetic stray field H_{tip} and the magnetic momentum m_{tip}), which showed a good consistency with the approximated values provided by the producer, demonstrating the efficiency of the procedure. The capability of accurately calibrating the magnetic behavior of the used probe allowed us to convert the magnetic phase values measured in correspondence of single NPs to the corresponding values of NP magnetization and to obtain the magnetization curves of single NPs as a function of the applied magnetic field, which represented one of the main open issues in the field of MFM-based characterization techniques. The proposed measurement and data analysis procedure has been tested on four Fe_3O_4 NPs having diameters in the range $21-32$ nm, the measured saturation magne-

tization and coercivity values of which resulted in good agreement with the corresponding values found in the literature and with the values we measured, on the same NPs, through a SQUID analysis. Reporting the results on only four nanoparticles cannot be considered a full validation and further studies aimed at validating the method, e.g., evaluation of the limit of detection and quantification (LoD and LoQ, respectively), accuracy, repeatability, and lateral resolution, are currently ongoing. Nonetheless, the results reported in this work represent an intrinsically remarkable methodological outcome. Indeed, it is possible to conclude that, despite further analysis are needed to better evaluate the method, our CM-MFM technique has been demonstrated to be effective to perform real quantitative magnetic characterization at the nanometer scale and, in particular, on a challenging sample as single superparamagnetic nanoparticles, showing its high potentiality as a simple, not expensive, user-friendly and widely applicable nanomagnetometry tool.

Acknowledgements

The authors thank Dr. D. Fioriani (ISM-CNR) for useful discussion and E. Patrizi for technical assistance in magnetization measurements.

References

1 S. Karmakar, S. Kumar, R. Rinaldi and G. Maruccio, *J. Phys. Conf. Ser.*, 2011, **292**, 012002.
2 S. C. N. Tang and I. M. C. Lo, *Water Res.*, 2013, **47**, 2613–2632.
3 Q. A. Pankhurst, J. Connelly, S. K. Jones and J. Dobson, *J. Phys. D: Appl. Phys.*, 2003, **36**, R167–R181.
4 Q. A. Pankhurst, N. T. K. Thanh, S. K. Jones and J. Dobson, *J. Phys. D: Appl. Phys.*, 2009, **42**, 224001.
5 Y.-W. Jun, J.-W. Seo and J. Cheon, *Accounts Chem. Res.*, 2008, **41**, 179–189.
6 S. Laurent, D. Forge, M. Port, A. Roch, C. Robic, L. Vander Elst and R. N. Muller, *Chem. Rev.*, 2008, **108**, 2064–2110.
7 J. L. Dormann, D. Fiorani and E. Tronc, *Advances in Chemical Physics*, John Wiley & Sons, Inc., 2007, vol. 98, pp. 283–494.
8 A. G. Kolhatkar, A. C. Jamison, D. Litvinov, R. C. Willson and T. R. Lee, *Int. J. Mol. Sci.*, 2013, **14**, 15977.
9 Z. Karimi, L. Karimi and H. Shokrollahi, *Mater. Sci. Eng. C*, 2013, **33**, 2465–2475.
10 L. C. Branquinho, M. S. C. ao, A. S. Costa, N. Zufelato, M. H. Sousa, R. Miotto, R. Ivkov and A. F. Bakuzis, *Sci. Rep.*, 2013, **3**, 2887.
11 S. Mørup, M. F. Hansen and C. Frandsen, *Beilstein J Nanotechnol.*, 2010, **1**, 182–190.
12 D. Peddis, P. E. Jönsson, S. Laureti and G. Varvaro, *Nanomagnetism: Fundamentals and Applications*, Elsevier, 2014, vol. 6, ch. 4, pp. 129–188.
13 D. Fiorani and D. Peddis, *J. Phys. Conf. Ser.*, 2014, **521**, 012006.
14 M. M. Saari, K. Sakai, T. Kiwa, T. Sasayama, T. Yoshida and K. Tsukada, *J. Appl. Phys.*, 2015, **117**, 17B321.
15 J. Hu, I. M. C. Lo and G. Chen, *Sep. Purif. Technol.*, 2007, **56**, 249–256.
16 A. L. Urbano-Bojorge, N. Félix-González, T. Fernández, F. del Pozo-Guerrero, M. Ramos and J. J. Serrano-Olmedo, *J. Nano Res.*, 2015, **31**, 129–137.
17 M. Brands, R. Wieser, C. Hassel, D. Hinzke and G. Dumpich, *Phys. Rev. B*, 2006, **74**, 174411.
18 A. Fernández-Pacheco, J. M. De Teresa, A. Szkudlarek, R. Córdoba, M. R. Ibarra, D. Petit, L. O'Brien, H. T. Zeng, E. R. Lewis, D. E. Read and R. P. Cowburn, *Nanotechnology*, 2009, **20**, 475704.
19 J. Schoenmaker, A. D. dos Santos, A. C. Seabra, Y. Souche, J.-P. Jamet, A. Thiaville and J. Ferre, *J. Appl. Phys.*, 2005, **98**, 086108.
20 T. Uhlig and J. Zweck, *Ultramicroscopy*, 2004, **99**, 137–142.
21 J. M. Thomas, E. T. Simpson, T. Kasama and R. E. Dunin-Borkowski, *Acc. Chem. Res.*, 2008, **41**, 665–674.
22 E. Snoeck, C. Gatel, L. M. Lacroix, T. Blon, S. Lachaize, J. Carrey, M. Respaud and B. Chaudret, *Nano Lett.*, 2008, **8**, 4293–4298.
23 S. Eisebitt, J. Lüning, W. F. Schlotter, M. Lörgen, O. Hellwig, W. Eberhardt and J. Stöhr, *Nature*, 2004, **432**, 885–888.
24 E. Amaladass, B. Ludescher, G. Schütz, T. Tyliszczak and T. Eimüller, *Appl. Phys. Lett.*, 2007, **91**, 172514.
25 P. Fischer, T. Eimüller, G. Schütz, G. Denbeaux, A. Pearson, L. Johnson, D. Attwood, S. Tsunashima, M. Kumazawa, N. Takagi, M. Köler and G. Bayreuther, *Rev. Sci. Instrum.*, 2001, **72**, 2322–2324.
26 D.-H. Kim, P. Fischer, W. Chao, E. Anderson, M.-Y. Im, S.-C. Shin and S.-B. Choe, *J. Appl. Phys.*, 2006, **99**, 08H303.
27 A. K. Geim, S. V. Dubonos, J. G. S. Lok, I. V. Grigorieva, J. C. Maan, L. T. Hansen and P. E. Lindelof, *Appl. Phys. Lett.*, 1997, **71**, 2379–2381.
28 L. Theil Kuhn, A. K. Geim, J. G. S. Lok, P. Hedegård, K. Ylänen, J. B. Jensen, E. Johnson and P. E. Lindelof, *Eur. Phys. J. D*, 2000, **10**, 259–263.
29 S. K. H. Lam, *Supercond. Sci. Technol.*, 2006, **19**, 963–967.
30 S. K. H. Lam, W. Yang, H. T. R. Wiogo and C. P. Foley, *Nanotechnology*, 2008, **19**, 285303.
31 C. Granata, E. Esposito, A. Vettoliere, L. Petti and M. Russo, *Nanotechnology*, 2008, **19**, 275501.
32 L. Hao, D. Cox, P. See, J. Gallop and O. Kazakova, *J. Phys. D Appl. Phys.*, 2010, **43**, 474004.
33 F. Kronast, N. Friedenberger, K. Ollefs, S. Gliga, L. Tati-Bismaths, R. Thies, A. Ney, R. Weber, C. Hassel, F. M. Römer, A. V. Trunova, C. Wirtz, R. Hertel, H. A. Dürr and M. Farle, *Nano Lett.*, 2011, **11**, 1710–1715.
34 O. Sandig, J. Herrero-Albillos, F. M. Römer, N. Friedenberger, J. Kurde, T. Noll, M. Farle and F. Kronast, *J. Electron Spectrosc. Relat. Phenom.*, 2012, **185**, 365–370.
35 L. Angeloni, D. Passeri, M. Reggente, M. Rossi, D. Mantovani, L. Lazzaro, F. Nepi, F. De Angelis and M. Barteri, *AIP Conf. Proc.*, 2015, **1667**, 020010.
36 D. Passeri, C. Dong, M. Reggente, L. Angeloni, M. Barteri, F. A. Scaramuzzo, F. De Angelis, F. Marinelli, F. Antonelli, F. Rinaldi, C. Marianecci, M. Carafa, A. Sorbo, D. Sordi, I. W. C. E. Arends and M. Rossi, *Biomatter*, 2014, **4**, e29507.
37 T. M. Nocera, J. Chen, C. B. Murray and G. Agarwal, *Nanotechnology*, 2012, **23**, 495704.
38 C. Moya, Óscar Iglesias-Freire, N. Pérez, X. Batlle, A. Labarta and A. Asenjo, *Nanoscale*, 2015, **7**, 8110–8114.
39 S. Schreiber, M. Savla, D. V. Pelekhov, D. F. Iscru, C. Selcu, P. C. Hammel and G. Agarwal, *Small*, 2008, **4**, 270–278.
40 E. Pinilla-Cienfuegos, S. Kumar, S. Mañas-Valero, J. Canet-Ferrer, L. Catala, T. Mallah, A. Forment-Aliaga and E. Coronado, *Part. Part. Syst. Char.*, 2015, **32**, 693–700.
41 M. Ranjbar, S. Piramanayagam, D. Suzi, K. O. Aung, R. Sbiaa, Y. S. Kay, S. K. Wong and C. T. Chong, *IEEE T. Magn.*, 2010, **46**, 1787–1790.
42 J. K. W. Yang, Y. Chen, T. Huang, H. Duan, N. Thiyagarajah, H. K. Hui, S. H. Leong and V. Ng, *Nanotechnology*, 2011, **22**, 385301.
43 W. L. Pei, G. W. Qin, Y. P. Ren, S. Li, T. Wang, H. Hasegawa, S. Ishio and H. Yamane, *Acta Mater.*, 2011, **59**, 4818–4824.
44 C. C. Chen, J. Y. Lin, L. Horng, J. S. Yang, S. Isogami, M. Tsunoda, M. Takahashi and J. C. Wu, *IEEE T. Magn.*, 2009, **45**, 3546–3549.
45 M. R. Tabasum, F. Zighem, J. De La Torre Medina, A. Encinas, L. Piraux and B. Nysten, *J. Appl. Phys.*, 2013, **113**, 183908.
46 M. R. Tabasum, F. Zighem, J. De La Torre Medina, A. Encinas, L. Piraux and B. Nysten, *Nanotechnology*, 2014, **25**, 245707.
47 J. Jin Park, M. Reddy, B. J. H. Stadler and A. B. Flatau, *J. Appl. Phys.*, 2013, **113**, 17A331.
48 M. Jaafar, L. Serrano-Ramón, O. Iglesias-Freire, A. Fernández-Pacheco, M. R. Ibarra, J. M. De Teresa and A. Asenjo, *Nanoscale Res. Lett.*, 2011, **6**, 407.
49 M. V. Rastei, R. Meckenstock and J. P. Bucher, *Appl. Phys. Lett.*, 2005, **87**, 222505.
50 M. Coïsson, G. Barrera, F. Celegato, E. Enrico, A. Manzin, E. S. Olivetti, P. Tiberto and F. Vinai, *J. Phys. D: Appl. Phys.*, 2014, **47**, 325003.
51 S. Sievers, K. F. Braun, D. Eberbeck, S. Gustafsson, E. Olsson, H. W. Schumacher and U. Siegner, *Small*, 2012, **8**, 2675–2679.
52 G. Cordova, S. Attwood, R. Gaikwad, F. Gu and Z. Leonenko, *Nano Biomed. Eng.*, 2014, **23**, 31–39.
53 T. Häberle, F. Haering, H. Pfeifer, L. Han, B. Kuerbanjiang, U. Wiedwald, U. Herr and B. Koslowski, *New J. Phys.*, 2012, **14**, 043044.
54 M. Jaafar, O. Iglesias-Freire, L. Serrano-Ramón, M. R. Ibarra, J. M. de Teresa and A. Asenjo, *Beilstein J. Nanotechnol.*, 2011, **2**, 552–560.
55 A. Schwarz and R. Wiesendanger, *Nano Today*, 2008, **3**, 28–39.
56 V. Cambel, D. Gregušová, P. Eliáš, J. Fedor, I. Kostič, J. Maňka and P. Ballo, *J. Electr. Eng.*, 2011, **62**, 37–43.
57 Y. Wang, Z. Wang, J. Liu and L. Hou, *Scanning*, 2015, **37**, 112–115.
58 L. Angeloni, D. Passeri, M. Reggente, D. Mantovani and M. Rossi, *Sci. Rep.*, 2016, **6**, 26293.
59 L. Angeloni, D. Passeri, F. A. Scaramuzzo, D. Di Iorio, M. Barteri, D. Mantovani and M. Rossi, *AIP Conf. Proc.*, 2016, **1749**, 020006.
60 H. Iida, K. Takayanagi, T. Nakanishi and T. Osaka, *J. Colloid Interf. Sci.*, 2007, **314**, 274–280.
61 H. M. Lu, W. T. Zheng and Q. Jiang, *J. Phys. D Appl. Phys.*, 2007, **40**, 320.
62 M. A. Vergés, R. Costo, A. G. Roca, J. F. Marco, G. F. Goya, C. J. Serna and M. P. Morales, *J. Phys. D Appl. Phys.*, 2008, **41**, 134003.
63 G. F. Goya, T. S. Berquó, F. C. Fonseca and M. P. Morales, *J. Appl. Phys.*, 2003, **94**, 3520–3528.
64 G. Muscas, G. Concas, C. Cannas, A. Musinu, A. Ardu, F. Orrù, D. Fiorani, S. Laureti, D. Rinaldi, G. Piccaluga and D. Peddis, *J. Phys. Chem. C*, 2013, **117**, 23378–23384.